




# Driving asymmetric red supergiant winds with binary interactions

Camille Landri   and Ondřej Pejcha 

*Institute of Theoretical Physics, Faculty of Mathematics and Physics, Charles University, V Holešovičkách 2, 180 00 Praha 8, Czech Republic*

Accepted 2024 May 29. Received 2024 May 27; in original form 2024 April 26

## ABSTRACT

Massive stars in the red supergiant (RSG) phase are known to undergo strong mass-loss through winds and observations indicate that a substantial part of this mass-loss could be driven by localized and episodic outflows. Various mechanisms have been considered to explain this type of mass-loss in RSGs, but these models often focus on single-star evolution. However, massive stars commonly evolve in binary systems, potentially interacting with their companions. Motivated by observations of the highly asymmetric circumstellar ejecta around the RSG VY CMa, we investigate a scenario where a companion on an eccentric orbit grazes the surface of an RSG at periastron. The companion ejects part of the outer RSG envelope, which radiatively cools, reaching the proper conditions for dust condensation and eventually giving rise to dust-driven winds. Using simple treatments for radiative cooling and dust-driven winds, we perform three-dimensional smoothed particle hydrodynamic simulations of this scenario with a  $20 M_{\odot}$  RSG and a  $2 M_{\odot}$  companion. We follow the evolution of the binary throughout a total of 14 orbits and observe that the orbit tightens after each interaction, in turn enhancing the mass-loss of subsequent interactions. We show that one such grazing interaction yields outflows of  $3 \times 10^{-4} M_{\odot}$ , which later results in wide asymmetric dusty ejecta, carrying a total mass of  $0.185 M_{\odot}$  by the end of simulations. We discuss the implications for the evolution of the binary, potential observational signatures, as well as future improvements of the model required to provide sensible predictions for the evolution of massive binaries.

**Key words:** hydrodynamics – (stars:) binaries (including multiple): close – stars: massive – stars: mass-loss – stars: winds, outflows.

## 1 INTRODUCTION

The red supergiant (RSG) phase is an important part of the evolution of massive stars with initial masses between 8 and  $25 M_{\odot}$  (e.g. Ekström et al. 2012), during which they undergo substantial mass-loss through winds. Observations show that a significant part of this mass-loss can be driven by episodic outflows localized on the stellar surface (Humphreys et al. 2021), as is shown by the ejecta surrounding VY CMa. VY CMa is a RSG located at 1.2 kpc (Zhang et al. 2012) and is one of the largest and most massive RSGs observed to this date, with a current radius of  $1420 \pm 120 R_{\odot}$ , a luminosity of  $(2.7 \pm 0.4) \times 10^5 L_{\odot}$ , and an initial mass at the upper range for RSGs ( $25 - 32 M_{\odot}$ , Wittkowski et al. 2012). Various observations of VY CMa show that it is embedded in asymmetric circumstellar ejecta with distinct and complex structures such as arcs, knots, and clumps (Smith et al. 2001; Humphreys, Helton & Jones 2007; Jones et al. 2007; Kamiński et al. 2013; Richards et al. 2014; O’Gorman et al. 2015; Decin et al. 2016; Vlemmings et al. 2017; Gordon et al. 2019; Kaminski 2019; Humphreys et al. 2021; Quintana-Lacaci et al. 2023; Humphreys et al. 2024). The clumps, in particular, are thought to be caused by highly localized mass-loss events that have been occurring for the past 1200 yr (Shenoy et al. 2016), but their origin so far remains unexplained.

Various mechanisms have been considered to explain episodic mass-loss in single RSGs, generally involving dust-driven winds launched by a disturbance of the stellar surface by magnetic activity, convection, or pulsations (e.g. Smith et al. 2001; Humphreys et al. 2007; O’Gorman et al. 2015; Vlemmings et al. 2017). However, quantitative prescriptions of these processes are scarce and often ambiguous, and stellar evolution models of cool supergiants continue to use time-averaged empirical mass-loss formulations that do not take into account the episodic nature of RSG mass-loss (e.g. de Jager, Nieuwenhuijzen & van der Hucht 1988; Nieuwenhuijzen & de Jager 1990; van Loon et al. 2005). Since these localized outflows can represent a large fraction of the mass lost by the RSG, as is the case for VY CMa, our poor understanding of these mechanisms introduces large uncertainties in current massive star evolution models (e.g. Smith 2014) and serious discrepancies between theory and observations (e.g. Massey et al. 2023). Furthermore, a lot of important astrophysical processes, such as gravitational wave emission from compact binaries, chemical evolution of galaxies, and core-collapse supernovae (SNe), strongly depend on massive star evolution. It is therefore crucial to improve our understanding of episodic mass-loss in RSGs and better constrain their fate.

An important aspect of RSG evolution is multiplicity. A significant fraction of massive stars are found in binary systems (e.g. Mason et al. 2009; Sana et al. 2012; Moe & Di Stefano 2017), with a large variety of possible configurations, including some with short separation of the two stars which allow them to interact. A small but significant

\* E-mail: [camille.landri@utf.mff.cuni.cz](mailto:camille.landri@utf.mff.cuni.cz)

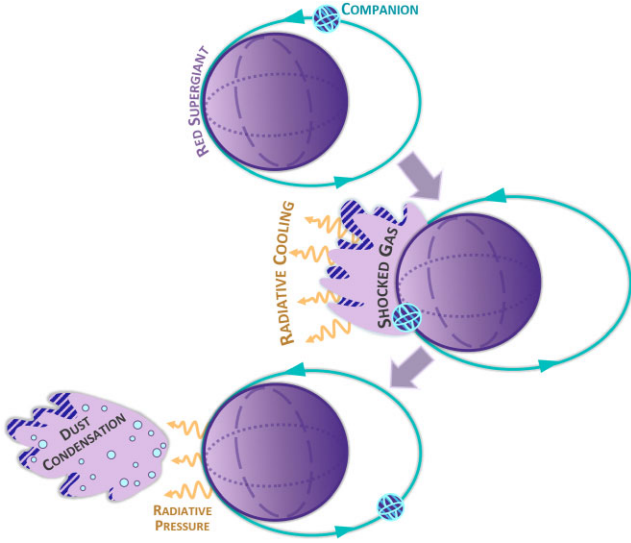


**Figure 1.** Schematics of the scenario explored with our simulations. A companion on an eccentric orbit grazes the envelope of the RSG and the resulting outflow radiatively cools, eventually reaching temperatures that permit dust formation. Radiation pressure then accelerates the dust grains, which drag the gas along, resulting in asymmetric dust-driven winds.

part of these systems are expected to remain bound and interact throughout their whole evolution, leading to the formation of objects such as X-ray binaries or gravitational wave events. For instance, common formation channels for double neutron star binaries show multiple evolution stages where one of the stars is an RSG interacting with its companion (e.g. Tauris et al. 2017). Therefore, scenarios where binary interaction and stellar winds interplay are likely to occur. While the impact of binarity on stellar winds has been investigated in the case of stars on the Asymptotic Giant Branch (AGB; e.g. Bermúdez-Bustamante et al. 2020; Chen, Ivanova & Carroll-Nellenback 2020; Aydi & Mohamed 2022; Esseldeurs et al. 2023), it remains widely unexplored for RSG stars.

In this paper, we investigate a scenario where binary interaction can drive anisotropic mass-loss episodes in RSGs that can later turn into dust-driven winds. More specifically, we consider an RSG with a companion grazing the RSG envelope on a highly eccentric orbit. We illustrate this scenario in Fig. 1: the companion grazes the outer envelope at each periastron passage and the shocked gas is ejected from the envelope. As the ejected gas spreads outwards, it cools and eventually reaches temperatures that are low enough to allow dust to condense. Radiative pressure then accelerates the newly formed dust grains, dragging the gas along and effectively driving an asymmetric wind. Eventually, the companion enters deep into the envelope of the RSG and commences a common envelope evolution (e.g. Paczynski 1976; Fragos et al. 2019; Lau et al. 2022; Gagnier & Pejcha 2023; Röpkke & De Marco 2023; Gagnier & Pejcha 2024). This scenario resembles the grazing envelope evolution proposed by Soker (2015) except we do not involve accretion disc and jets around the companion and the resulting outflow morphology is different (Shiber, Kashi & Soker 2017). Our model makes use of radiation pressures on dust grains, which was suggested as important in the late stages of common envelope evolution by Glanz & Perets (2018). Glanz & Perets (2021) also studied common envelope evolution in eccentric binaries but did not address anisotropic outflows during periastron passages.

We explore the proposed scenario through three-dimensional (3D) hydrodynamic simulations, where we include a simplified treatment of dust formation and radiation pressure driving the RSG outflows. We note that the aim of this proof-of-concept study is not to reproduce the detailed properties and complicated morphology of the ejecta surrounding VY CMa or other RSGs, where in reality they likely arise from an interplay of many different processes. Instead, our goal is to illustrate that binary interactions can potentially explain some of the observed features. A more sophisticated treatment of dust formation and radiative processes can be added in follow-up studies to reach a better agreement with the observations. In Section 2, we describe the methods used to model our scenario, including how we simplified the different treatments of the physical processes involved. In Section 3, we present our results, including the evolution of the orbit, amounts of mass ejected, and the ejecta expansion. In Section 4, we discuss the possible formation channels for our system, the implications of our model for binary evolution, the possible observational signatures of such winds, and future improvements for our models.

## 2 METHODS

We use the smoothed particle hydrodynamic (SPH) code PHANTOM (Price et al. 2018) that solves the Lagrangian form of the equations of hydrodynamics by discretizing the fluid as particles with mass  $m$  and local fluid velocity  $v$  (e.g. Gingold & Monaghan 1977; Lucy 1977; Price 2012). Physical quantities are then computed by summing particle contributions weighted by a smoothing kernel  $W$ , for instance, the density around particle  $a$  is given by

$$\rho_a = \sum_b m_b W(|\vec{r}_a - \vec{r}_b|, h_a), \quad (1)$$

where  $h_a$  is the smoothing length, which defines the neighbourhood of the particle  $a$ , and is proportional to the local particle number density  $n_a = h_{\text{fact}} n_a^{-1/3}$ ,  $h_{\text{fact}}$  is a proportionality factor. The resolution of the simulations is therefore set by the total number of particles used, the choice of smoothing kernel and  $h_{\text{fact}}$ .

For this work, we set up PHANTOM to solve the equations of hydrodynamics in the following form:

$$\frac{d\vec{v}}{dt} = -\frac{\nabla P}{\rho} + \pi_{\text{shock}} + \vec{a}_{\text{selfgrav}} + \vec{a}_{\text{ext}}, \quad (2)$$

$$\frac{du}{dt} = -\frac{P}{\rho} (\nabla \cdot \vec{v}) + \Psi_{\text{shock}} - \frac{\Upsilon_{\text{cool}}}{\rho}, \quad (3)$$

where  $P$  is the pressure,  $u$  is the internal energy,  $\vec{a}_{\text{selfgrav}}$  is the acceleration due to self-gravity,  $\vec{a}_{\text{ext}}$  represents the acceleration due to external forces such as sink particles or a radiative flux,  $\pi_{\text{shock}}$  and  $\Psi_{\text{shock}}$  are viscous dissipation terms, and  $\Upsilon_{\text{cool}}$  is an optional cooling term. For  $W$ , we use the  $M_4$  cubic spline kernel with  $h_{\text{fact}} = 1.2$ , corresponding to an average of 58 neighbours.

Our scenario involves more than hydrodynamics and self-gravity. As shown in Fig. 1, our simulations require a treatment of radiative cooling as the shocked gas is ejected from the RSG and a treatment of dust condensation and radiative pressure to accelerate the outflow. Since this work is meant to be a proof of principle, these treatments will remain simple, but we do plan on improving them in follow-up studies. For this study, we run a set of four simulations which are summarized in Table 1. In the rest of this section, we describe how we initialize the RSG and the binary system (Section 2.1), as well as how we treat dust-driven winds (Section 2.3) and radiative cooling (Section 2.2).

**Table 1.** Summary of the simulations performed for this study, showing the number of particles, minimum softening length  $h_a$ , and processes involved in the run.

Number of particles	min $h_a$	Physics involved
$2.5 \times 10^5$	$22 R_\odot$	Hydro, self-gravity, cooling, dust-driven winds
$1 \times 10^6$	$14 R_\odot$	Hydro, self-gravity, cooling, dust-driven winds
$1 \times 10^6$	$14 R_\odot$	Hydro, self-gravity, adiabatic, no wind
$2 \times 10^6$	$11 R_\odot$	Hydro, self-gravity, cooling, dust-driven winds

## 2.1 Initialization of the system

We consider a binary of mass ratio  $q = M_2/M_1 = 0.1$  with a  $M_1 = 20 M_\odot$  RSG similar to VY CMa, and a companion of  $M_2 = 2 M_\odot$ , which could represent either a low-mass non-degenerate star or a fairly massive neutron star (NS; e.g. Özel & Freire 2016). We initialize this system in two steps, first, the one-dimensional (1D) stellar profile of the RSG is mapped to 3D and relaxed in PHANTOM. During this phase, there are no external accelerations and no cooling. Then, after ensuring the stability of the 3D model, we add the companion and let the binary evolve for several orbital periods.

For the interior of the RSG, we create a 1D stellar profile with properties similar to VY CMa, which has mass and radius estimated to be  $17 \pm 8 M_\odot$  and  $1420 \pm 120 R_\odot$ , respectively (Wittkowski et al. 2012). Since the companion mostly interacts with the outer layers of the RSG, it is unnecessary and computationally expensive to resolve the core and inner envelope of the giant. We therefore replace part of the stellar interior with a sink particle, a point mass that interacts with other particles only gravitationally through a potential smoothed with a cubic spline kernel. We excised about half of the envelope, which increases the number of particles at the stellar surface for a reasonable total number of particles as well as maintains a reasonable time-step during the simulations. For the rest of the envelope, we choose to use an artificial RSG profile that is convectively stable, since reproducing accurate convective motion requires resolving the inner envelope and we wish to avoid the decrease in time-step associated with these dense envelope layers. To create the model for the envelope, we follow the method provided in appendix A of Lau et al. (2022) and solve the equations of hydrostatic equilibrium with an ideal gas equation of state assuming an adiabatic index of  $\gamma = 5/3$ , constant entropy, and accounting for the softened potential of the core. To solve these equations, we used boundary conditions from a realistic RSG profile obtained with MESA (Paxton et al. 2011; Paxton et al. 2013, 2015, 2018, 2019; Jermyn et al. 2023) made to match the properties of VY CMa (for a detailed description of the process see the Appendix).

Following this process, we created a 1D convectively stable profile of a  $20 M_\odot$  and  $1500 R_\odot$  RSG that is shown in Fig. 2. We initialized it in PHANTOM with a sink particle core of  $13.75 M_\odot$  and a potential smoothed with a cubic spline kernel. We define the smoothing length of this potential to be  $R_{\text{soft},1} = 375 R_\odot$ , yielding an effective radius of  $750 R_\odot$  for the sink particle since the Newtonian potential is recovered at  $2r_{\text{soft}}$  with a cubic spline kernel. The 1D stellar profile of the RSG is mapped to a 3D distribution and then relaxed using the procedure implemented in PHANTOM by Lau et al. (2022). The giant is then evolved for 10 dynamical time-scales ( $\tau_{\text{dyn}} = 241 d$ ) to ensure the stability of the star. In Fig. 2, we show the density profile before and after relaxation: while the RSG remains stable, the relaxation and subsequent evolution yield a small change in stellar radius as the RSG has slightly expanded during the relaxation and then contracted.

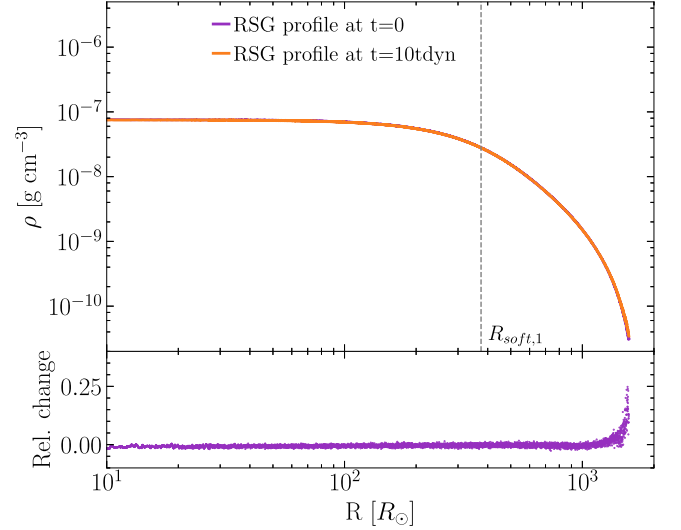


**Figure 2.** Density profile of the outer envelope of the RSG in our simulation at the end of the relaxation and  $10 \tau_{\text{dyn}}$  later. Top: Density profiles, purple shows the initial profile and orange the profile after  $10 \tau_{\text{dyn}}$ , the grey dashed line shows the softening radius of the RSG numerical core. Bottom: Relative change in density computed as  $(\rho_f - \rho_i)/\rho_i$ . The envelope remains stable apart from a 25 per cent increase in density at the surface.

For the highest resolution simulation ( $2 \times 10^6$  particles), the RSG has expanded from  $1500 R_\odot$  to  $1569 R_\odot$ .

Once the star is relaxed and stable, we add the neutron star companion by placing it at the apoastron of the orbit. Since a neutron star is much smaller than the minimum smoothing length in our simulations, we initialize it as a sink particle of mass  $M_2 = 2 M_\odot$  with smoothing length and accretion radius equal to the minimum resolved length, which is  $R_{\text{soft},2} = 11 R_\odot$  for our highest resolution simulations with  $2 \times 10^6$  particles. The orbit of the system is set with a semimajor axis  $A = 7500 R_\odot$  and eccentricity  $e = 0.8$ , so that the secondary grazes the envelope of the RSG at each periastron passage. We then evolve the system for several orbits until the companion has plunged deeply into the RSG envelope and the smoothed potential of the two sink particles overlap.

## 2.2 Cooling

As the companion goes through the envelope of the giant, the shocked gas that is ejected becomes optically thin and cools radiatively to the local equilibrium temperature  $T_{\text{eq}}$ , where radiative cooling and irradiation from the RSG compensate each other. Under the assumptions of spherical symmetry and that the RSG radiative intensity dominated the local intensity,  $T_{\text{eq}}$  is given by (Lamers & Cassinelli 1999):

$$T_{\text{eq}} = T_{\text{eff},1} W(\tilde{r})^{1/(4+p_{\text{dust}})}, \quad W(\tilde{r}) = \frac{1}{2} \left( 1 - \sqrt{1 - \left( \frac{R_1}{\tilde{r}} \right)^2} \right), \quad (4)$$

where  $T_{\text{eff},1}$  and  $R_1$  are the effective temperature and radius of the RSG,  $\tilde{r}$  is the distance from the centre of mass of the RSG, and  $W(\tilde{r})$  is the so-called geometrical dilution factor. Since we are primarily interested in situations where  $T_{\text{eq}}$  decreases below the dust condensation temperature  $T_{\text{cond}}$ , equation (4) includes dust correction through the exponent  $p_{\text{dust}}$ , which comes from approximating the

wavelength-dependent part of the dust opacity with a power law,

$$\kappa_d = \kappa_0 \left( \frac{\lambda}{\lambda_0} \right)^{-p_{\text{dust}}}. \quad (5)$$

The dust properties are described in Section 2.3.

Since cooling impacts the kinematics of the ejected gas, it is important to take it into account in our simulations. The most natural way to handle this process would of course be to fully resolve radiative cooling and irradiation by imposing a cooling time-scale over which the gas relaxes to  $T_{\text{eq}}$ . The cooling time-scale  $t_{\text{cool}}$  over which a shocked gas radiates away its internal energy  $U = 3/2k_B T$  can be estimated from a radiative cooling function (e.g. fig. 22 of Ferland et al. 2017),

$$t_{\text{cool}} = \frac{U m_p}{\rho \Lambda(T)}. \quad (6)$$

Here,  $m_p$  is the proton mass,  $\rho$  is the density of the gas, and  $\Lambda(T)$  is the usual cooling function. As the companion goes through the envelope of the giant, the shocked upper layers of the envelope reach temperatures up to 35 000 K, for which the cooling rate is approximately  $3.16 \times 10^{-4} \text{ erg cm}^3 \text{ s}^{-1}$ . For a density of  $10^{-10} \text{ g cm}^{-3}$ , equation (6) yields  $t_{\text{cool}} \approx 3.2 \times 10^{-4} \text{ s}$ . Considering the hydrodynamical time-step  $t_{\text{step}}$  of our simulations is of the order of hours, it is impossible to resolve such fast cooling in our simulations without making their cost unreasonably high.

We therefore have to resort to a simpler method to cool the ejected gas. Instead of imposing a time-scale for the cooling process, the ejected particles are cooled so that they would exponentially reach  $T_{\text{eq}}$  on a time-scale equal to the hydrodynamical time-step. This ensures that cooling does not become faster than the explicit time-step and should prevent the development of cooling instabilities. To do so, the equilibrium temperature at a particle location  $T_{\text{eq},a}$  is calculated using equation (4), and the corresponding specific internal energy is obtained using the ideal gas equation of state:

$$u_{\text{eq},a} = \frac{k_b T_{\text{eq},a}}{(\gamma - 1) \mu m_p}, \quad (7)$$

where the adiabatic index is  $\gamma = 5/3$  and the mean molecular weight is  $\mu = 0.659$ . The local cooling rate per unit volume is then calculated as

$$\Upsilon_{\text{cool},a} = \rho \frac{u_a - u_{\text{eq},a}}{t_{\text{step}}}, \quad (8)$$

where  $u_a$  is the specific internal energy of the particle before cooling is applied. This cooling rate is applied in equation (3) for any particle that is considered ‘ejected’, i.e. is outside of the RSG envelope,

$$\Upsilon_{\text{cool}} = \begin{cases} \Upsilon_{\text{cool},a} & \text{if } \tilde{r}_a > R_1, \\ 0 & \text{if } \tilde{r}_a \leq R_1. \end{cases} \quad (9)$$

To avoid approaching too low temperatures, we apply an arbitrary floor temperature of 500 K. Overall, our treatment of the radiative cooling process is an oversimplification and will require more accurate treatment in follow-up studies.

### 2.3 Dust-driven winds

In our scenario, the wind is driven by the radiation pressure on the dust condensing in the ejecta lifted by the companion passage. As the dust grains are accelerated outward by the radiative flux, they drag the gas along by transferring momentum through collisions. Accurately reproducing the formation of such winds therefore requires resolving dust formation (and destruction), the radiative acceleration of dust

grains, and dust-gas interactions. As this work aims to be a proof of concept, we will treat this problem with simple methods that should yield qualitatively similar outcomes to more complete physical treatments. We leave the improvement of the wind treatment for follow-up studies.

The radiative acceleration of the dust grains due to the radiative flux of the RSG is taken into account by setting  $\vec{a}_{\text{ext}}$  in equation (2) so that it depends on a local Eddington factor  $\Gamma_a$ ,

$$\vec{a}_{\text{ext,rad}} = \frac{GM_1}{r_1^2} \Gamma_a \hat{r}_a, \quad (10)$$

where  $\hat{r}_a$  is the unit vector connecting particle  $a$  to the RSG. The simplest treatment of stellar winds is the so-called free wind approximation (Theuns & Jorissen 1993), which consists of setting  $\Gamma_a = 1$  so that all particles escape the gravitational pull of the star. We apply this method to our simulations, adding the condition that only particles with properties fulfilling dust condensation criteria are accelerated. To find out whether dust can condense in a specific region, we compare the condensation temperature of the dust  $T_{\text{cond}}$  to the temperature of the particle  $T_a$  and set the value of  $\Gamma_a$  as

$$\Gamma_a = \begin{cases} 1 & \text{if } T_a < T_{\text{cond}}, \\ 0 & \text{if } T_a > T_{\text{cond}}. \end{cases} \quad (11)$$

We set the dust properties following Bladh & Höfner (2012) who parametrized dust-driven winds for different types of dust grains to determine the main wind-drivers. Based on their results and the low C/O ratio of RSG stars, we consider silicate grains composed of  $\text{Mg}_2\text{SiO}_4$ , for which they derived  $T_{\text{cond}} = 1100 \text{ K}$  and  $p_{\text{dust}} = -0.9$ . The dust parameters we note that with this formalism, we do not account for the interaction between the dust and gas, which are effectively fully coupled.

Overall, our method is similar to the procedure devised by Bowen (1988), which has been widely used to treat dust condensation in AGB stellar winds (e.g. Bermúdez-Bustamante et al. 2020; Chen et al. 2020; Aydi & Mohamed 2022; Esseldeurs et al. 2023) and common envelope evolution (e.g. González-Bolívar et al. 2022; Bermúdez-Bustamante et al. 2024), but it differs in some aspects. Their simulations are always adiabatic, so they compare the local equilibrium temperature (calculated using equation [4]) to the condensation temperature, whereas in our simulations the gas cools as it is ejected, and we can directly use the gas temperature for the comparison. Additionally, they use this comparison to calculate a local Eddington factor  $\Gamma$  that depends on the temperature difference and assumptions on gas and dust opacities, while we simply apply  $\Gamma = 1$  wherever dust condensation conditions are met.

## 3 RESULTS

We performed a total of four simulations: three runs with cooling, dust driving and varying resolution ( $2.5 \times 10^5$ ,  $1 \times 10^6$ , and  $2 \times 10^6$  particles), and one control adiabatic run without cooling and dust-driven winds with  $1 \times 10^6$  particles. The parameters of the runs are summarized in Tables 1 and 2.

In Fig. 3, we show snapshots of the density cross-section in our highest resolution simulation during the first grazing of the RSG envelope. As the companion grazes the outermost layers of the envelope, the shocked gas is ejected approximately perpendicularly to the stellar surface. However, it is then dragged by the companion as it leaves the vicinity of the RSG. Eventually, the outflow expands approximately radially in the  $y < 0$  region, while we observe no ejection of gas in the  $y > 0$  region. The outflow expands and cools, reaching the dust condensation temperature  $T_{\text{cond}} = 1100 \text{ K}$

**Table 2.** Initial conditions of the high-resolution simulations ( $2 \times 10^6$  particles).  $T_{\text{cond}}$  and  $p_{\text{dust}}$  are the dust condensation parameters according to equations (4) and (5).

RSG primary	$M_1$	20.0 $M_{\odot}$
	$R_1$	1569 $R_{\odot}$
	$R_{\text{soft},1}$	375 $R_{\odot}$
	$M_{\text{core}}$	13.75 $M_{\odot}$
	$M_{\text{env}}$	6.25 $M_{\odot}$
	$T_{\text{eff}}$	3500 K
Companion	$M_2$	2.0 $M_{\odot}$
	$R_{\text{soft},2}$	11 $R_{\odot}$
Binary	Eccentricity	0.8
	Semimajor axis	7500 $R_{\odot}$
	Period	43.91 yr
Dust	$T_{\text{cond}}$	1100 K
	$p_{\text{dust}}$	-0.9

for  $r \gtrsim 4500 R_{\odot}$ , where the gas density is about  $10^{-14} \text{ g cm}^{-3}$ . Radiative pressure then starts to accelerate the dust grains, effectively supporting the radial expansion of the gas. During the following orbit, the outflow continues expanding while the RSG, which first expanded as a response to the perturbation from the companion, is restoring its hydrostatic equilibrium. After one full orbit (around 40 yr), the outflow has extended to a rough semicircle of radius  $r \sim 400 \text{ au}$  in the  $xy$  plane with a thickness of  $z \sim 200 \text{ au}$ , reaching densities as low as  $10^{-18} \text{ g cm}^{-3}$  and terminal velocities of around  $40 \text{ km s}^{-1}$ . Besides producing these asymmetric winds, we also expect the interaction

between the companion and the RSG envelope to impact the orbit of the system, which in turn impacts the conditions of each subsequent grazing.

To assess the relevance of the cooling and the dust-driven winds in supporting the asymmetric outflows, we performed a fully adiabatic simulation. In Fig. 4, we show the outflow resulting from one grazing interaction after the companion has passed the apastron in both the adiabatic and non-adiabatic simulations. We see that the ejecta in the adiabatic simulation is much more extended: it reaches  $r \gtrsim 500 \text{ au}$  with a thickness of  $\sim 300 \text{ au}$ , while the radiatively cooled ejecta has only spread to  $r \sim 200 \text{ au}$  with a thickness of  $\sim 200 \text{ au}$ . Additionally, the adiabatic outflow is denser, reaching up to  $10^{-14} \text{ g cm}^{-3}$  in the inner region, against  $10^{-15} - 10^{-16} \text{ g cm}^{-3}$  for the cooled outflow. Finally, the asymmetry of the ejecta with respect to the centre of mass of the system is much less pronounced in the adiabatic case: the adiabatic outflow broadly surrounds the RSG, while the gas is only ejected in a roughly semicircular slab in the simulations with cooling and winds. This comparison shows that the cooling and wind prescriptions are essential to produce strongly asymmetric outflows.

### 3.1 Evolution of the orbit

As the companion grazes the RSG envelope, we expect the drag between the gas and the companion to considerably affect the orbit of the binary. In Fig. 5, we show the evolution of the separation of the binary. We see that during each subsequent periastron passage, the companion reaches deeper layers of the outer envelope and the orbit tightens while remaining eccentric. The binary starts with a

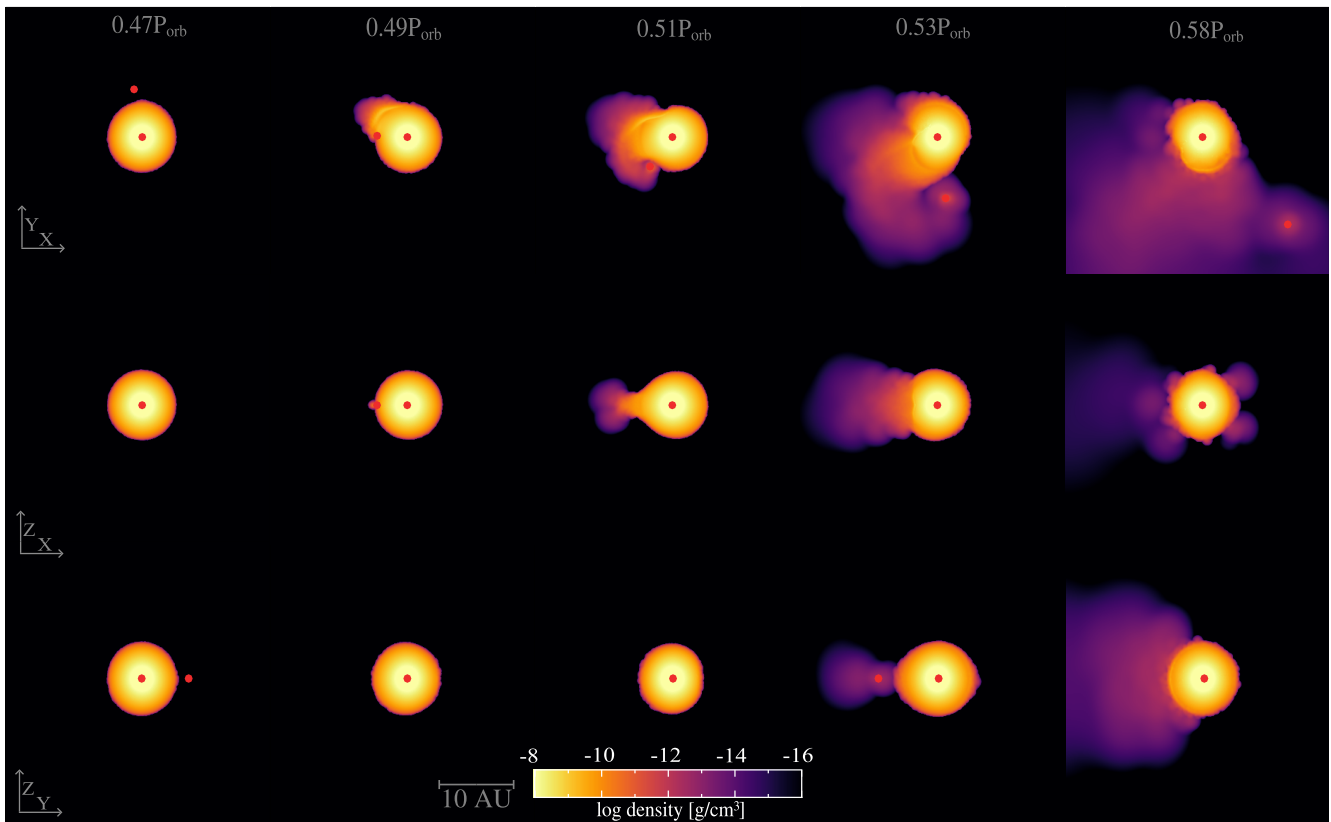


**Figure 3.** Snapshots of the density during the first periastron passage in our highest resolution run ( $2 \times 10^6$  particles). The upper, middle, and lower panels show cross-sections of density taken at  $z = 0$ ,  $y = 0$ , and  $x = 0$  planes, respectively. Sink particles are denoted as red circles. A full movie of the first interaction can be found at <https://youtu.be/jcW0KyMayBE>.

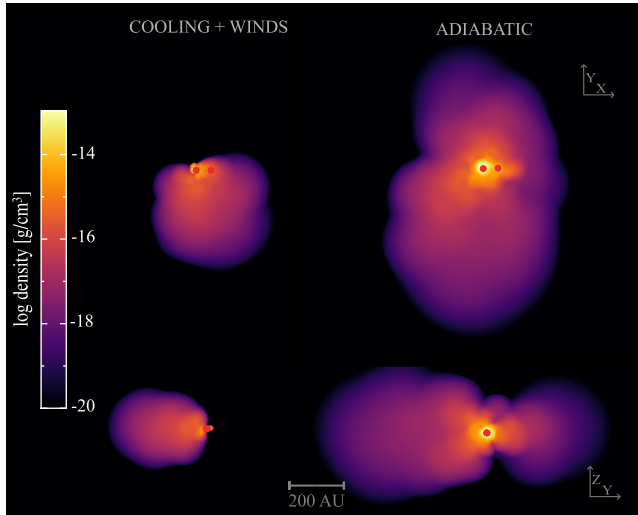


**Figure 4.** Comparison of the ejecta after one apastron passage of the companion for the adiabatic run (right panels) and a run with radiative cooling and dust-driven winds (left panels). The upper and lower panels show a cross-section of the density taken along the  $z = 0$  and  $x = 0$  planes, respectively. Both simulations were performed with  $1 \times 10^6$  particles.

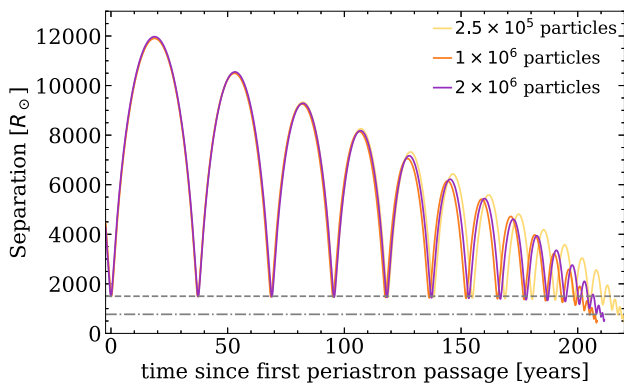


**Figure 5.** Evolution of the binary separation. The high, medium, and low-resolution runs are shown in purple, orange, and yellow, respectively. The upper and lower dashed lines show the RSG surface ( $1500 R_{\odot}$ ) and the sum of the effective radii of the two sink particles for the high-resolution run ( $772 R_{\odot}$ ).

$\sim 40$  yr period, which decreases on average by 3–4 yr after each orbit, reaching a period of about 7 yr on the 10th orbit. At this point, the companion is more than  $250 R_{\odot}$  beneath the RSG surface at periastron, driving more massive and less localized outflows, and decreasing the orbital period even faster.

After 13 orbits, the companion is fully engulfed by the RSG and starts spiralling in the envelope with a period of the order of one year, effectively starting a phase of common envelope evolution (CEE; e.g. Paczynski 1976; Röpke & De Marco 2023). Unfortunately, we cannot resolve the inspiral of the companion in our simulations: the potential of the RSG sink core is smoothed up to  $750 R_{\odot}$ , so we barely observe one full orbit of the inspiral before the smoothed potentials of the sink particles overlap, at the end of the 13th orbit. We expect that more mass will be ejected during CEE, and the outflow should retain some polar asymmetry until the CEE circularizes the orbit. It is however not possible to determine the outcome of the CEE with our simulations.

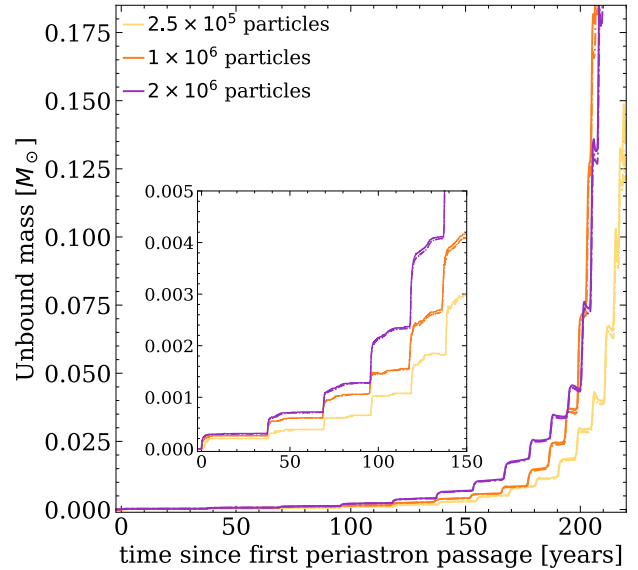


**Figure 6.** Evolution of the amount of unbound mass. The high, medium, and low-resolution runs are shown in purple, orange, and yellow, respectively. Plain lines show the amount of unbound mass according to the energy criterion in equation (13), which includes the gas’ internal energy, dashed lines show the amount of unbound mass using the more conservative energy criterion in equation (12), which does not include internal energy. The inner plot shows the mass-loss during the first orbits.

Overall, the orbit of the binary tightens drastically throughout the simulation due to the grazing interaction, leading to CEE after only 200 yr. We discuss implications and possible modifications to this time-scale in Section 4.

### 3.2 Mass-loss

We estimate the mass lost by the system after each periastron passage using the usual energy criteria: a particle is considered unbound if its kinetic energy is higher than its gravitational energy,

$$E_{\text{gr}} + E_{\text{kin}} > 0. \quad (12)$$

Alternatively, a fraction of the internal energy of the gas,  $\alpha E_{\text{int}}$ , can be converted into kinetic energy, and the amount of unbound particles is then determined as

$$E_{\text{gr}} + E_{\text{kin}} + \alpha E_{\text{int}} > 0. \quad (13)$$

Since  $\alpha$  is unconstrained, setting it to unity allows us to derive an upper limit on the mass-loss of the binary, while the more conservative criteria set by equation (12) can serve as a lower limit. Using both criteria, we evaluate the evolution of the mass-loss throughout the simulations, which we show in Fig. 6.

During the first three orbits, the mass-loss is very episodic, with a sharp rise in the total unbound mass of  $\sim 3 \times 10^{-4} M_{\odot}$  right after each grazing interaction. Between interactions, the amount of unbound mass stays essentially constant. Most of the ejected particles have been cooled, radiatively accelerated, and unbound within a year from the periastron passage of the companion. Then, from the fourth orbit onward, the sudden rise in mass-loss becomes stronger and the unbound mass is rising continuously. Both of these features intensify after each subsequent interaction. Since the surface layers of the RSG expand in response to the grazing interaction, and the companion reaches deeper and denser layers of the envelope, it drives more massive episodic outflows at periastron, but also a low-intensity

continuous outflow until the next interaction. About  $10^{-3} M_{\odot}$  of mass is unbound 1–2 yr after the interaction, and about  $10^{-4} M_{\odot}$  is lost continuously in between each periastron passage. After the 10th orbit, the system approaches CEE and episodically ejects  $\gtrsim 10^{-2} M_{\odot}$  per interaction. The companion is completely engulfed by the envelope after the 13th orbit and ejects about  $0.1 M_{\odot}$  of matter in a continuous way. At the end of the simulation, which corresponds to a total of 14 orbits, the system has ejected a total of  $0.185 M_{\odot}$ , 80 per cent of which was ejected in the last 10 yr of the evolution, during the onset of CEE.

We note that our estimation of the mass ejected during the late evolution of our system is flawed due to our simplified treatments of cooling and dust condensation. Our treatment of radiative cooling does not take gas opacities into account since it relies on the approximation that the ejected gas is optically thin. However, this assumption does not hold for the outflows launched when the system is close to the onset of CEE, which should be optically thicker considering their high density. The opacity of these outflows likely decreases as they expand, but they will become optically thin and start to radiatively cool at much larger distances from the system than earlier outflows. Therefore, our method underestimates the temperature of the late outflows, allowing dust to condense and radiation pressure to drive winds in regions where it is not likely to happen. This leads to an overestimation of the outflow velocities and possibly of the amount of unbound mass at late times.

Fig. 6 also shows that the differences between the two mass-loss criteria are relatively insignificant, especially at early times when the two criteria yield practically the same result. This is expected, since the internal energy of the gas at the stellar surface is much lower than the kinetic energy imparted to the gas by the companion during the interaction and any extra thermal energy from shock interaction is quickly radiated. After five orbits, however, the companion starts to probe deeper layers of the envelope, with increasingly higher internal energy and where our cooling prescription is not active, so the two estimates deviate from one another. As the end of the simulation approaches, the gap between the two values deepens and we expect the difference between the two criteria to be similarly significant during the ensuing CEE phase.

### 3.3 Evolution of the ejecta

In Fig. 7, we track the evolution of the ejecta on longer time-scales by showing density snapshots of our highest resolution simulation during subsequent orbits at the moment of apastron. Each successive periastron passage of the companion drives a new outflow, which first increases the density of the inner ejecta, then expands and merges with the less dense outer part of the ejecta. In this section, we use the term ‘ejecta’ to qualify the entire body of ejected gas and the term ‘outflow’ for the gas ejected due to one grazing interaction only.

The evolution of the ejecta can be broadly divided into two phases that mostly differ by the time elapsed between subsequent grazing interactions. For the first five orbits, the orbital period ranges from 40 to 20 yr and the outflows can expand over large scales before the binary is at periastron again, which causes the broad spiral pattern in the ejecta appearing in the first row of Fig. 7. This slow evolution lasts for about 140 yr, during which the ejecta expands to  $r \gtrsim 1000$  au as a roughly semicircular slab of vertical thickness  $\sim 500$  au, with densities ranging from  $10^{-15}$  g cm $^{-3}$  in the innermost region to  $10^{-19}$  g cm $^{-3}$  in the outer ejecta.

As seen in Fig. 5, each interaction strengthens the orbital decay of the binary, which starts to strongly affect the outflows after the fifth

orbit of the binary. At this point, the grazing interactions become more frequent, with a period  $P_{\text{orb}} \leq 20$  yr, causing tighter spiral patterns in the inner ejecta while the ejecta continues spreading outwards. The companion also starts to dig deeper into the envelope of the RSG, significantly increasing the density of each subsequent outflow, reaching up to  $10^{-13}$  g cm $^{-3}$  in the innermost part of the ejecta. As the system approaches the onset of CEE, we also see that matter is ejected more isotropically, and the densest part of the outflow spreads around the binary with a shape similar to a disc. We expect that the outflows will become even more isotropic as the system evolves through CEE since the orbit should circularize, but the already ejected material should retain its overall asymmetry.

At the end of the simulation, the dusty ejecta broadly resembles a cone and we can distinguish three main regions. First, the innermost region, directly surrounding the binary, results from the late time evolution during which the binary was close to the onset of CEE and the outflows are the most massive. With a total mass of about  $0.15 M_{\odot}$  extending up to  $\sim 100$  au away from the binary in a roughly conical shape, it is by far the densest region of the ejecta. Since the time elapsed between grazing interactions has drastically decreased, the shell-like overdensities caused by the companion shocking the gas are closer to each other, yielding a tighter spiral pattern than in earlier stages of the simulation. Beyond the innermost ejecta, we identify a relatively dense region of  $10^{-15}$ – $10^{-17}$  g cm $^{-3}$  spreading up to  $\sim 500$  au from the system, which we estimate to carry  $\sim 3 \times 10^{-2} M_{\odot}$ . This region is more asymmetric than the inner ejecta, it corresponds to where most of the outflows have merged and is thus made of the most extended parts of the late evolution outflows and the slowest regions of earlier outflows. Finally, a wide and less dense region extends to  $r \gtrsim 2000$  au, with densities reaching very low values of  $10^{-18}$ – $10^{-20}$  g cm $^{-3}$ . This region carries roughly  $5 \times 10^{-3} M_{\odot}$ , corresponding to the early outflows that have now spread far away from the binary.

In Fig. 8, we show the radial velocity of the gas at the end of the simulation. The late outflows can be traced in the spiral pattern by sharp velocity fronts, while the early outflows have softer velocity gradients as they merged a long time ago. The outermost ejecta, arising from the first outflows and spreading beyond  $r \gtrsim 500$  au, show radial velocities of  $v_r \sim 50$ – $60$  km s $^{-1}$ . The rest of the ejecta has not reached such high velocities, the innermost part has on average  $v_r \lesssim 30$  km s $^{-1}$  while the intermediate region reaches  $v_r \approx 40$  km s $^{-1}$ . We, therefore, estimate the wind terminal velocity to be  $v_{\infty} \approx 60$  km s $^{-1}$ .

## 4 DISCUSSIONS

Here, we discuss constraints on the evolutionary pathways that lead to the grazing by the companion (Section 4.1), statistics of binarity of RSGs (Section 4.2), the duration of the grazing phase (Section 4.3), what happens after the interaction (Section 4.4), observational signatures (Section 4.5), and possible future improvements of our model (Section 4.6).

### 4.1 Formation of the system

The evolutionary pathways leading to our configuration depend on whether the RSG companion is a compact object, such as a neutron star, or a low-mass non-degenerate companion. From the point of view of our simulations, both options are indistinguishable, because the gravitational potential of the companion must be smoothed on scales larger than its radius. If the companion is a low-mass main sequence (MS) star, the binary could have simply been born on this

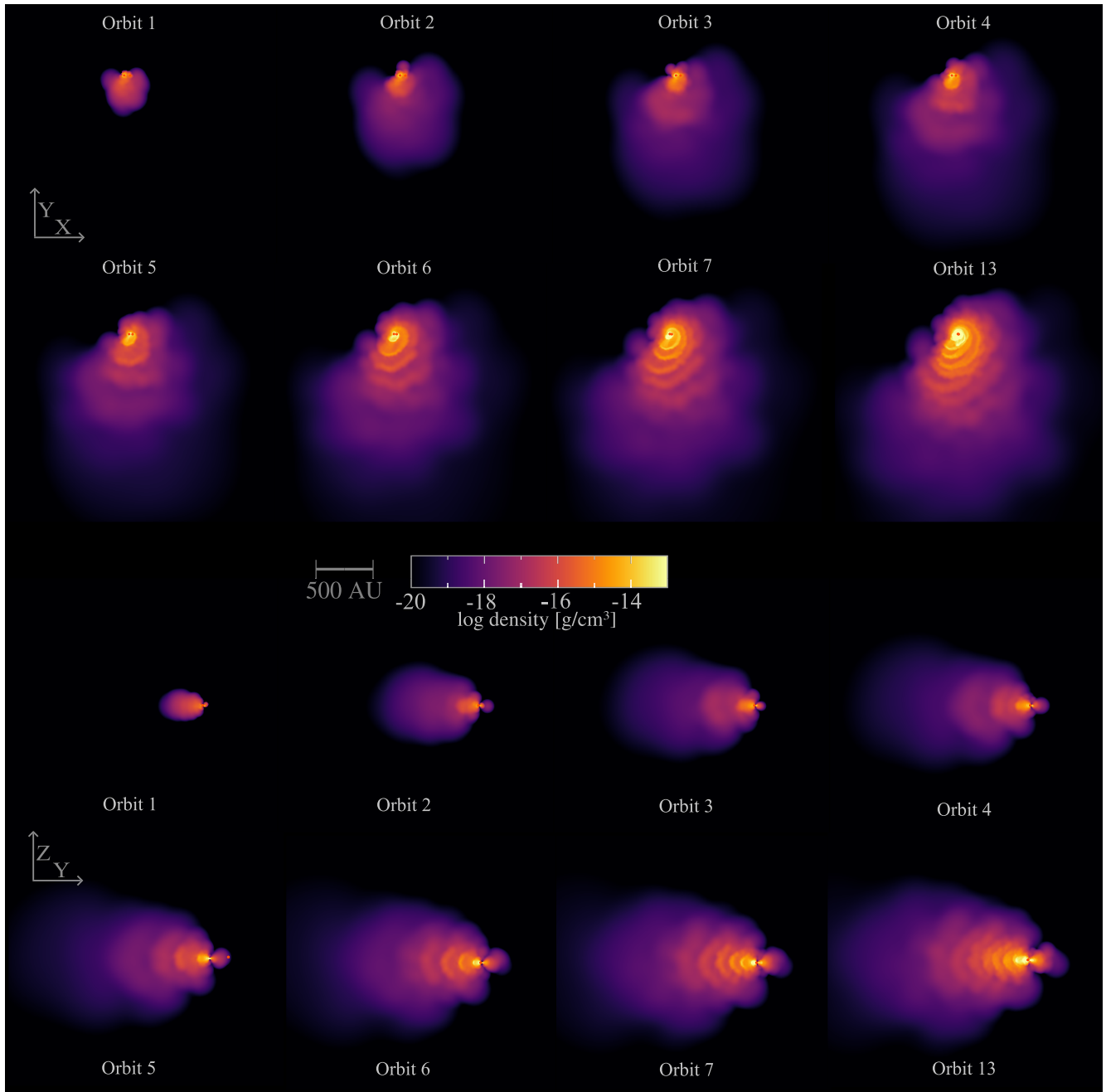


**Figure 7.** Density snapshots of the simulation with  $2 \times 10^6$  particles taken when the companion is at apastron. The two upper rows show the density cross-section of the equatorial plane (slice along  $z = 0$ ) and the two bottom rows show the meridional plane (slices along  $x = 0$ ).

orbit and began interacting when the more massive star expanded to an RSG. Alternatively, the binary has such a low mass ratio that it may have formed in a wider more circular orbit and was subject to the Darwin and/or eccentric instability (e.g. Darwin 1879; Hut 1980; Eggleton & Kiseleva-Eggleton 2001; Peřta & Pejcha 2023), which would have reduced the binary separation and potentially increased its eccentricity. Considering that VY CMa is associated with but lies off of a cluster NGC 2362 (Lada & Reid 1978; Mel’Nik & Dambis 2009; Zhang et al. 2012), it is interesting to speculate about a scenario where a massive star in a binary explodes as a supernova, leaves behind a neutron star, and the explosion kick sets the neutron star on an eccentric orbit and the binary on a trajectory away from

its birth cluster. While this scenario might not apply to VY CMa specifically, it is interesting to discuss it more generically.

We consider a common scenario for the formation of double neutron star binaries (Tauris et al. 2017), starting with two massive MS stars on a relatively close orbit. The more massive star eventually evolves and expands, and the binary experiences a phase of case B or C mass transfer. As the RSG transfers mass to its companion, it is gradually stripped of its envelope and eventually undergoes core collapse (CC). The collapsing star turns into an NS without fully disrupting the binary, which according to Renzo et al. (2019) should happen in about 14 percent of massive binaries. While the natal kick of the NS does not fully unbind the binary, it will increase



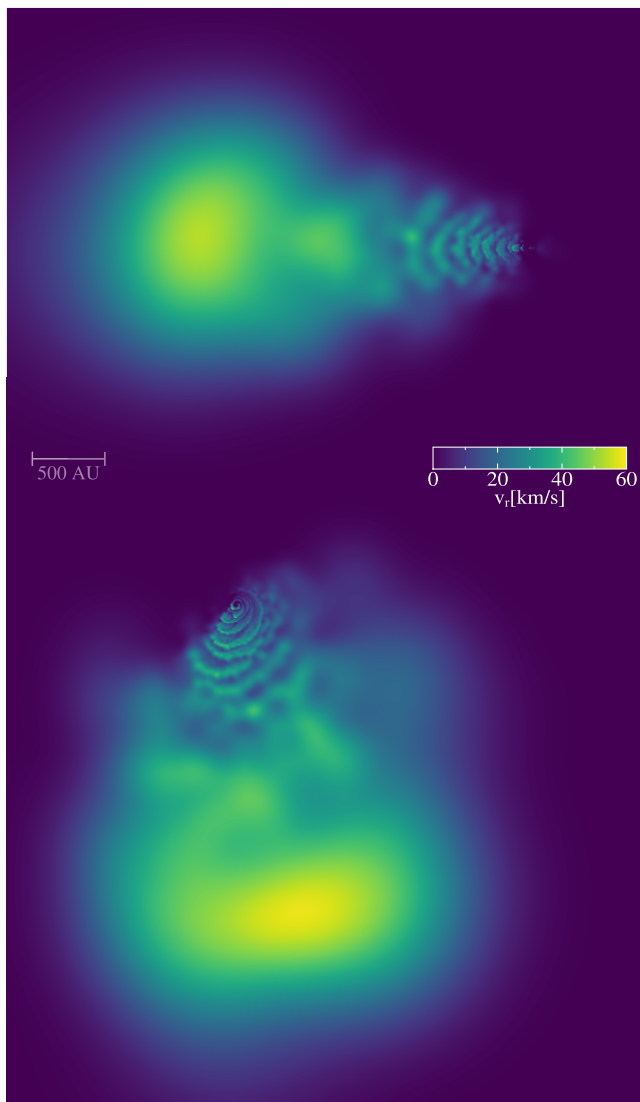


**Figure 8.** Snapshot of the radial velocity of the ejecta taken after 14 orbits. The upper and lower panels show radial velocities taken at  $x = 0$  and  $z = 0$  planes, respectively.

its eccentricity (Brandt & Podsiadlowski 1995; Kalogera 1996) and widen the orbit to up to 4 times the pre-CC separation according to Kalogera (1996). The initially less massive star will expand to an RSG, eventually reaching radii large enough for the compact companion to graze the RSG envelope at periastron.

The time-scale of the post-CC evolution depends on how close the initial masses of the two stars were and whether the accretion during the pre-CC mass transfer phase has increased the main-sequence lifetime of the accretor (Neo et al. 1977). It is, however, strictly constrained by the tidal circularization time-scale of the binary (Zahn 1977), since the star should reach the RSG phase before the eccentricity of the binary decreases significantly. If we consider that the initially less massive star is close to the onset of the RSG phase at the birth of the NS, and therefore has a significantly convective envelope, the circularization time-scale of the binary is highly dependent on the ratio of semimajor axis to stellar radius  $\tau_{\text{circ}} \propto (A/R_1)^8$ . Using equation (2) of Verbunt & Phinney (1995), the circularization time-scale reaches a maximum estimate of  $\tau_{\text{circ}} \simeq 10^7 \text{ yr}$  for a  $20 M_{\odot}$ ,  $1500 R_{\odot}$  RSG. The binary should thus

circularize on longer time-scales than the time-scale of the evolution and expansion of the future RSG, which should be at most of the order of  $10^6 \text{ yr}$  if the star is still on the MS at the start of the post-CC evolution. Therefore, the binary should retain its large eccentricity by the time the compact companion can graze the envelope of the RSG.

## 4.2 Statistics of RSG binarity

Statistics of RSG binarity can serve as a clue as to whether our scenario occurs frequently. Neugent et al. (2018) devised some criteria to detect companions around RSGs from their contribution in the spectra of the binaries, however, they are mostly efficient for blue companions since their contamination is more easily distinguished from the red light of the RSG. A complementary way of determining the binarity of a RSG is to secure multiepoch spectroscopy to look for periodic variations of radial velocities. However, due to the large radii of RSGs the minimum orbital period of their companion has to be of the order of hundreds of days, meaning that such spectroscopic studies have to be performed on time-scales of years. Furthermore, the amplitude and time-scale of these periodic variations are likely similar to the variability due to atmospheric convective motion in RSGs (Schwarzschild 1975), which further complicates RSG multiplicity studies. Despite these difficulties, the binary fraction of cool supergiants in the Milky Way has been estimated to be around 35 per cent (Burki & Mayor 1983), and some X-ray binaries were found to have a RSG companion (e.g. Gottlieb et al. 2020; Hinkle et al. 2020). RSG multiplicity studies targeting the Local Group (e.g. Neugent et al. 2019; Patrick et al. 2019; Neugent et al. 2020; Dorda & Patrick 2021; Neugent 2021) generally find binary fractions around 30 per cent, mostly with OB-type companions. Patrick et al. (2022) found 6 candidates for RSG + compact companion in the Small Milky Cloud, though they potentially are false positives, and Neugent (2021) estimated the fraction of RSG + compact companion in M31 and M33 to be about 4.73 per cent using BPASS (Eldridge et al. 2017). While rates of binarity for RSGs inferred from observations are relatively low, especially for binaries with a compact companion, it is still non-negligible and therefore our grazing scenario seems plausible.

## 4.3 Duration of the grazing encounters

Our simulations cover only about 200 yr or 13 orbits before the binary enters the CEE. Such a short duration would imply that our chances of finding a RSG undergoing this type of evolution are very slim given the RSG lifetime. However, the duration of our simulation is mostly driven by the constraints of available computing time and resolution. If both can be increased, we could simulate the evolution for many more orbits before the CEE. This interaction is similar to a normal CEE, where Iaconi et al. (2018) and Reichardt et al. (2019) found that increasing simulation resolution leads to a longer duration of pre-CEE inspiral, mass transfer, and mass-loss. The long duration of the pre-dynamical CEE phase is also seen in 1D binary evolution simulations (e.g. Klennicki et al. 2021; Marchant et al. 2021). Observations of transients accompanying stellar mergers, the luminous red novae, also indicate the presence of pre-dynamical mass-loss lasting many hundreds and potentially thousands of binary orbits (e.g. Tylenda et al. 2011; Pejcha, Metzger & Tomida 2016a, b; Pejcha et al. 2017; Blagorodnova et al. 2021).

Another aspect affecting the duration of the grazing phase is missing physics near the surface layers of the star. Real stars exhibit a complex interplay of convection, diffusion, and ionization in their

surface layers, which affects the stability with respect to mass removal (e.g. Pavlovskii & Ivanova 2015). In RSGs specifically, the additional physical effects include the large size of convective cells, pulsations leading to in the outer atmosphere shocks, dust and molecule formation in the gas lifted off the surface by pulsations, and feedback from accretion on to the companion (e.g. Haubois et al. 2009; Shiber & Soker 2018; Goldberg, Jiang & Bildsten 2022; Freytag & Höfner 2023).

All of these effects could extend the duration of the grazing phase by making the conditions in the outer stellar layers different from what we assume in our adiabatic simulations. Furthermore, the mass ejections could happen intermittently depending on whether the periastron passage occurs during the maximum or minimum expansion of the RSG pulsation. Finally, a longer duration of the grazing phase could also facilitate precession and tilting of the companion orbit, for example, due to the action of tidal forces. The mass ejections would then still be oriented in one direction during each ejection or a series of subsequent ejections, but the orientation of the ejection could gradually change. All of these aspects would be interesting to investigate in future work.

#### 4.4 Evolution and fate of the binary

Depending on the amount of envelope ejected during the CEE ensuing after the grazing and the nature of the companion, the system could evolve to a close binary with two compact objects (e.g. a double NS binary, Tauris et al. 2017), or the two stars could merge, possibly resulting in a Thorne-Żytkow object (ZTO; Thorne & Żytkow 1977) if the companion is an NS, or an exotic supernova if the merger product explodes (e.g. Chevalier 2012). It is, however, not possible to draw conclusions on the outcome of this process from our simulations, since properly simulating this phase of the evolution of the binary would require resolving the deep interior of the RSG.

We may broadly examine the outcome of the CEE using the energy formalism (e.g. Webbink 1984):

$$-G \frac{M_1 M_{1,e}}{\lambda R_1} = -\alpha_{CE} E_G \left[ \frac{M_{1,c} M_2}{2A_f} - \frac{M_1 M_2}{2A_i} \right], \quad (14)$$

where  $M_{1,e}$  and  $M_{1,c}$  are the mass of the RSG envelope and core, respectively, which are about 13.5 and 6.5  $M_\odot$  according to the MESA model used to set up our RSG. Parameter  $\lambda$  is defined by the mass distribution inside the star,  $A_i$  and  $A_f$  and the initial and final separation of the CEE. By setting  $\alpha_{CE}$ , the envelope ejection efficiency, and  $\lambda \lesssim 0.1$  as appropriate for evolved RSGs (Kruckow et al. 2016), we find that the CEE can unbind the whole envelope for final separation of  $A_f \lesssim 4R_\odot$ . Thus, it seems unlikely that the system ejects the whole envelope. This estimation is however too simple to reflect the reality since the efficiency of envelope ejection in CEE and the physical processes involved (e.g. recombination, dust formation) are still relatively unconstrained in current CEE models (see Röpke & De Marco 2023 for a detailed discussion). Therefore, we leave the fate of the binary as an open question.

We can, however, estimate the impact of our chosen initial conditions on the evolution of the system. We could consider a companion mass  $M_2$  lower than 2  $M_\odot$ , in which case we expect less massive outflows due to the grazing interaction. In our simulations, the efficiency of the radiative force to drive the winds would remain unchanged due to the very simple formulation of radiative pressure on dust grains; therefore, we do not expect the wind velocities to change for a different companion mass. However, we note that in a realistic scenario, the efficiency of dust condensation does depend on the density of the gas, and since a lower mass companion yields

less dense outflow, it would also likely change the wind properties. The decrease in companion mass would also cause the orbit to decay more slowly, as the dynamical friction between the outer envelope and the companion is lower during each periastron passage, which will result in a later plunge-in. We expect opposite effects for higher companion masses: more massive outflows and a faster evolution.

The choice of orbital parameters of the system should also have a significant influence on the evolution of the binary and the outflows. In our simulations,  $a$  is not freely chosen, it is set so that the binary separation at periastron is exactly equal to the radius of the RSG,  $a = R_1/(1 - e)$ . For lower  $e$ ,  $a$  is smaller and the less eccentric orbit will be overall closer to the RSG surface. As a result, the companion grazes a larger portion of the stellar surface and encounters higher densities. This leads to less asymmetric outflows, and the higher drag on the companion accelerates the orbital decay to CEE.

#### 4.5 Observational signatures

Here, review various observations that can indicate that grazing encounters are ongoing or happened relatively recently: outflow emission, changes of the RSG, accretion on to companion, observable signatures of TZO, and supernova explosions. We also specifically discuss VY CMa.

##### 4.5.1 Outflow emission

The most evident signature of this interaction is the emission from the cool asymmetric outflow, which we expect to be observable at millimetre/submillimetre and infrared wavelengths. As shown in Fig. 7 the dusty outflow could be angularly resolved with the ALMA interferometer if the distance to the system is small enough. Outside of the continuum emissions from the dust, the ejecta should also be traceable with molecular emissions, which arise from the various gas-phase chemistry across the outflow. Since we do not model the various phenomena occurring at the RSG surface, the morphology of the outflow in our simulations represents the simplest possible outcome. However, any complicated morphological feature in the outflow would likely be unresolvable, which includes the spiral features in the innermost ejecta, and traces of the common envelope phase would likely be hard to detect.

##### 4.5.2 Changes of the RSG

Repeated close passages of a companion will affect the RSG by tidal dissipation. Our simulations are inadequate to study these processes, but we can speculate about some of the potential outcomes. First, the RSG could expand in response to the tidal heating. For our choice of companion mass, the orbital energy of a grazing orbit is much smaller than the RSG envelope binding energy (Klencki et al. 2021) and no significant overall expansion is expected. However, the dissipated energy could still strengthen the processes that are already ongoing such as the more common dust-driven RSG wind, potentially leading to a tidally enhanced wind (e.g. Tout & Eggleton 1988; Chen, Han & Tout 2011). The intensity of this effect depends on the amount of tidal dissipation, the depth of deposition, and the ability of the star to quickly remove this excess energy by radiation.

##### 4.5.3 Accretion on to companion

Before fully entering the envelope of the RSG, our system should also show X-ray emission from the accretion on the companion.

Since the companion moves supersonically through the outflow of the RSG, we can approximate the accretion rate  $\dot{M}_2$  of the companion using the approximation of spherical accretion on to a moving object (Bondi–Hoyle–Lyttleton–Lyttleton accretion),

$$\dot{M}_2 = \frac{4\pi\rho(GM_2)^2}{(c_s^2 + v_2^2)^{3/2}}, \quad (15)$$

where  $\rho$  is the density of the surrounding outflow,  $c_s$  is the sound speed,  $M_2$  the mass of the companion, and  $v_2$  is the velocity of the companion relative to the surrounding gas. In our simulations, the average relative velocity of the companion is  $20 \text{ km s}^{-1}$ , and the density of the surrounding ejecta is  $10^{-15} \text{ g cm}^{-3}$ , resulting in an accretion rate of  $4 \times 10^{-6} M_\odot$ . The corresponding accretion luminosity is  $L_{\text{acc}} = GM_2\dot{M}_2/R_2$  where  $R_2$  is the radius of the companion. Inefficient accretion or radiative emission will decrease  $L_{\text{acc}}$ . When considering a low-mass MS companion of  $R_2 \simeq 2R_\odot$ , the accretion luminosity becomes  $L_{\text{acc}} \simeq 10^{35} \text{ erg s}^{-1}$ , making it similar to X-ray bright T Tauri stars (Telleschi et al. 2007). For an NS companion of  $R_2 = 10 \text{ km s}^{-1}$ , the accretion rate yields a very high luminosity of  $L_{\text{acc}} \simeq 10^{40} \text{ erg s}^{-1}$ , which is a factor of  $\sim 50$  higher than the Eddington limit for a  $2 M_\odot$  star. Given the super-Eddington accretion rate, the NS might look like an ultra-luminous X-ray source displaying super-Eddington flux only near the polar axis (e.g. King 2009). If jets develop, our scenario reduces to the grazing envelope evolution developed by Soker (2015), Shiber et al. (2017), and Shiber & Soker (2018).

The high-gas density in the vicinity of the RSG that gives rise to a high  $\dot{M}_2$  also provides a large gas column that can absorb and scatter the X-rays. Considering a spherical constant-velocity outflow from the RSG with  $r^{-2}$  density profile,  $\dot{M}_1 = 10^{-5} M_\odot \text{ yr}^{-1}$ , velocity  $20 \text{ km s}^{-1}$ , and inner edge at  $1500 R_\odot$ , we obtain density  $\approx 10^{-15} \text{ g cm}^{-3}$  and hydrogen column of  $\sim 10^{23}$ . Depending on the emission temperature and the detector properties, such a high gas column can reduce the expected flux by many orders of magnitude (e.g. Montez et al. 2015). Even with inefficient accretion and a high intervening gas column, we would still expect signatures of accretion such as highly ionized gas or feedback on the surrounding medium.

#### 4.5.4 Observable signatures of TZO

As we discussed in Section 4.4, the companion could have spiralled in and merged with the core of the RSG, possibly resulting in a TZO. These objects are hard to distinguish from RSGs, only a few candidates have been proposed, such as U Aqr (Vanture, Zucker & Wallerstein 1999), HV 2112 (Levesque et al. 2014; Tout et al. 2014; Maccarone & de Mink 2016; Worley et al. 2016; Beasor et al. 2018), and VX Sgr (Taberner et al. 2021), and none of these objects have been confirmed to be TZOs. According to Cannon et al. (1992), a TZO should look like a cool and bright RSG close to the Hayashi limit (Hayashi & Hoshi 1961), but show unusual lines in its optical spectra. As the neutron star spirals in the envelope of its companion, the combination of the high surface temperature of the NS and convective envelope of the RSG would trigger interrupted rapid proton (irp) capture (Cannon 1993). Despite the broad TiO absorption features observed in RSGs, some of the heavier elements produced by the irp processes should have high enough abundances in the atmosphere to be observed, especially Rb, Yb, and Mo (Biehle 1994). Other TZO spectral features include  $^7\text{Li}$  and Ca I enhancement (Podsiadlowski, Cannon & Rees 1995; Tout et al. 2014) or  $^{44}\text{TiO}$  and  $^{44}\text{TiO}_2$  (Farmer et al. 2023).

#### 4.5.5 Supernova explosions

The merger of the RSG core and the companion may also result in a supernova explosion, which could produce a black hole remnant if the companion is a compact object. Many Type II<sub>n</sub> supernovae and other luminous transients show evidence for mass ejections preceding the terminal supernova explosion (e.g. Margutti et al. 2014; Ofek et al. 2014; Jacobson-Galán et al. 2022). It has been suggested that a strong binary interaction or a CEE is responsible for pre-supernova mass ejections leading to a formation of dense circumstellar medium (CSM; e.g. Smith 2011; Chevalier 2012; Metzger 2022). This has motivated theoretical works investigating interactions of supernova explosions with various aspherical CSM distributions such as disks, oblate or prolate ellipsoids, and colliding winds shells (e.g. Vlasis, Dessart & Audit 2016; Suzuki, Moriya & Takiwaki 2019; Kurfürst, Pejcha & Krtićka 2020; Pejcha, Calderón & Kurfürst 2022). Interestingly, none of these works has considered the type of aspherical CSM that we are predicting here: subtending only a small fraction of a solid angle with internal density variations corresponding to individual periastron passages. However, based on analogous works on different aspherical CSM distributions, we can predict that a supernova explosion colliding with the CSM predicted here would lead to a radiative shock that is quite likely embedded in the optically thick supernova ejecta and that initially reveals its presence only as an additional energy source. When the supernova ejecta becomes optically thin, the CSM distribution could manifest in profiles of nebular spectral lines.

#### 4.5.6 Application to VY CMa

We can compare these expected signatures to observations of VY CMa. We first note that no companion has been directly observed around VY CMa, suggesting that if our scenario was ever involved in the evolution of VY CMa, the companion is now either fully engulfed in the envelope of the supergiant or is orbiting too close to the stellar surface to be observable Decin et al. (2006) reconstructed the mass-loss history of VY CMa and found that it underwent a phase of increased mass-loss rate of  $\simeq 3 \times 10^{-4} M_\odot \text{ yr}^{-1}$  about 1000 yr ago. This phase lasted about 100 yr and was preceded by a phase with relatively low mass-loss rate of  $\simeq 10^{-6} M_\odot \text{ yr}^{-1}$  for about 800 yr and succeeded by a phase of increased mass-loss of  $\simeq 10^{-4} M_\odot \text{ yr}^{-1}$  lasting until today. It would be natural to identify this event of increased mass-loss with grazing interactions, which culminated with a stellar merger followed by an enhanced wind phase due to the energy deposition in the RSG envelope by the inspiralling companion (e.g. Clayton et al. 2017; Glanz & Perets 2018).

Alternatively, the morphology of our asymmetric outflow seems to be consistent with the dusty clumps observed in the immediate vicinity of VY CMa (e.g. Kaminski 2019). The mass of these clumps was estimated to be of the order of  $10^{-3}$ – $10^{-2} M_\odot$  with velocities of  $20$ – $50 \text{ km s}^{-1}$ , and were likely ejected about 100 yr ago (Humphreys et al. 2024), which is consistent with the total mass of the extended ejecta in our simulations and the velocities shown in Fig. 8. We note that our wind terminal velocities only depend on the Eddington factor, which is a free parameter set in equation (11), so they are a broad upper limit rather than a reliable estimate. Kaminski (2019) estimated the size of the clumps with 3D radiative transfer models, and found that the most elongated clump (clump B) could be up to 1000 au long, which is compatible with the size of our ejecta.

Concerning the companion accretion, Montez et al. (2015) obtained non-detections in X-rays that place an upper limit of  $L_X < 1.6 \times 10^{31} \text{ erg s}^{-1}$ , which is far below the estimated  $L_{\text{acc}} 10^{35} \text{ erg}$

$s^{-1}$  we derived. However, the upper limit is highly contingent on the emission temperature and the sensitivity to softer radiation with  $T \lesssim 10^6$  K is much worse given the expected intervening absorption column. Still, VY CMa does not prominently display highly ionized emission lines or other signs of an accretion process. So if VY CMa had a companion, it was probably already deep within the RSG envelope by the time the observations were made. If the companion is a NS then we might expect VY CMa to be a TZO, spectroscopic studies of the object do show Ca I and Rb I lines (Wallerstein 1971; Dinh-V-Trung et al. 2022); however, no traces of other heavy elements have been found. The use of different tracers, such as the ones proposed by Farmer et al. (2023), could shed some light on this issue.

To summarize, VY CMa could have merged with a grazing companion about 1000 yr ago; however, the complexity of its surrounding medium would require some modification to our model or combination with other physical processes. Increasing the realism of our model could allow to better determine whether this mechanism plays a role in the formation of some of the asymmetric outflows around VY CMa.

#### 4.6 Improvements of the model

Our simulations use approximations and simple treatments of the involved physical processes to reduce their computational cost. Here, we discuss potential improvements for follow-up studies.

First, we have made several assumptions regarding the initial conditions of our set-up. We have assumed that when the simulations start, no interactions are taking place between the RSG and the companion. Considering how close the two stars are, there is a chance that the RSG overfills its Roche Lobe around the periastron of one or more orbits preceding the start of the simulations, resulting in potential mass transfer and/or outflows. However, any interaction during the previous orbits would simply lead to smaller, possibly negligible, mass ejections. To assess the relevance of previous interactions, one could evolve the binary in 1D in MESA following the methods of Marchant et al. (2021), and possibly obtain better initial conditions for our simulations.

Another approximation we made in this study is to model the RSG envelope as convectively stable, which prevents us from investigating the interplay between surface convection and the companion interaction, which would likely affect the morphology of the ejecta. However, resolving convective motion requires modelling the entire RSG envelope as well as including radiative transport in the envelope, to avoid a strong overestimation of the convective flux (e.g. Ricker et al. 2018). Both choices would dramatically increase the cost of the simulations, especially considering the long time-scale of our simulations, therefore, incorporating convection in our simulations will likely be considered in later phases of improvements.

Furthermore, as mentioned in Sections 2.2 and 2.3, our numerical treatment of dust-driven winds has been simplified and can be improved to various degrees. Dust formation and destruction can be more accurately treated by including a density and composition dependence, for instance by using the moment method (Gail, Keller & Sedlmayr 1984; Gail & Sedlmayr 1988; Gauger, Gail & Sedlmayr 1990; Gail & Sedlmayr 2013), which has been implemented for carbonaceous dust grains in PHANTOM by Siess et al. (2022). RSG stars have a low C/O ratio, so this method would need to be adapted to oxygen-rich dust condensation, which is significantly harder to model than carbon-rich dust formation. There are many more dust species to account for compared to the case of carbon-rich dust, and

it is not completely known which particles serve as seed nuclei for oxygen dust growth (for more details, see chapter 15.5.6 of Gail & Sedlmayr 2013). Implementing a complete condensation scheme for oxygen-rich dust in 3D hydrodynamics codes is therefore a challenging but important step towards improving dust treatment in simulations of evolved stars. It would also allow for a better estimation of local opacities and Eddington factor, which are essential for the proper treatment of radiation pressure on the dust-gas mixture.

We could further improve the realism by resolving the dust-gas interactions. PHANTOM already has several formalisms for dust-gas mixtures, either with a two-fluid approach (Laibe & Price 2012) or a one-fluid method that keeps track of the composition of the mixture (Laibe 2014; Laibe & Price 2014; Price & Laibe 2015). While the outcome of simulations with accurate treatments of dust-driven winds might be qualitatively similar to our results, it would also likely yield a more detailed structure in the winds, and lower outflow velocity and densities since our dust condensation criterion is relatively permissive.

Improvements regarding the formulation of the radiative force on dust grains would also likely impact the morphology of the wind. Esseldeurs et al. (2023) shows the difference in radiative pressure treatments for winds in binaries with an AGB star, and it is clear that more accurate approximations (e.g. Lucy 1971, 1976) yield more detailed wind structures than with a simple free-wind approximation, as well as better estimations of the wind velocities. However, such methods require the calculation of optical depth, which needs to be estimated along the line of sight of each particle and severely complicates the simulations if one wants to calculate it on the fly during an SPH simulation. This was implemented in PHANTOM by Esseldeurs et al. (2023) using a ray tracer algorithm, so we leave the possibility of adapting their method to our set-up for follow-up studies.

## 5 CONCLUSIONS

The goal of this work was to investigate whether a companion grazing the envelope of a RSG can launch significant asymmetric episodic outflows that later expand through dust-driven winds. To do so, we performed 3D hydrodynamics simulations of a  $2 M_{\odot}$  star on a highly elliptical orbit around a  $20 M_{\odot}$  RSG with an envelope extending to  $1500 R_{\odot}$  (Fig. 1, Section 2). In our models, we see the companion grazing the RSG envelope at periastron and ejecting gas from the outermost envelope, which results in a dense semicircular outflow (Fig. 3). The ejected gas becomes optically thin and cools, reaching conditions that are favourable for dust condensation. The radiative pressure on dust grains then accelerates the outflow outwards, effectively launching dust-driven winds that expand radially.

We investigated the evolution of the system through several successive grazing interactions and found that the orbit drastically tightens after each interaction (Fig. 5). The orbital period decreases by  $\sim 3$ –4 yr per orbit, decreasing the periastron distance significantly and enhancing the mass-loss during the grazing interaction. The outflows therefore become denser and more frequent as the system evolves, effectively altering the properties of the ejecta (Fig. 7). The mass ejected during each grazing interaction goes from  $3 \times 10^{-4} M_{\odot}$  during to first orbit to  $\sim 10^{-2} M_{\odot}$  before the onset of CEE (Fig. 6).

After 13 orbits ( $\sim 200$  yr), the system enters CEE which dramatically enhances the orbital evolution and mass-loss rate of the binary. Due to the large softening length of the numerical core of the RSG, we cannot resolve the CEE of the system with our simulations; therefore, the outcome of the CEE remains unconstrained and could result in a short-period binary or a merger. Our simulations stop after

14 orbits, at which point the binary has ejected a total of  $0.185 M_{\odot}$  of gas spreading beyond  $r \gtrsim 1000$  au, with 80 per cent of this mass situated in the innermost part of the ejecta ( $r \lesssim 100$  au). The final ejecta has a conical shape and shows a shell-like structure due to the shocks from each grazing by the companion.

While the initial conditions of our simulation seem relatively exotic, mostly due to the eccentricity of the system, we expect this grazing interaction to be relevant for the evolution of massive binary systems. For instance, this scenario applies to binaries with low mass MS companions with an orbit wide enough to retain a significant eccentricity, in which the stars evolve as effectively single until the massive star expands as a RSG or the orbit dramatically tightens due to the Darwin instability.

Although the duration of this phase is uncertain and depends on complicated physics near the RSG surface, it should still produce observable signatures. The dusty ejecta should be observable at millimetre/sub-millimetre wavelengths, as well as molecular lines due to the rich chemistry expected in the outflow.

Additionally, the companion should accrete matter from the outflows, which we expect to result in X-ray emission or highly ionized lines. However, their detectability is highly affected by the large intervening absorption column expected in such situations.

Lastly, the binary could evolve to a TZO after CEE if the companion is an NS, which is of interest since TZOs are hard to distinguish from RSG, and none have been unambiguously identified yet.

By comparing our results with observations of the ejecta around VY CMa, we speculate that such a grazing interaction could have been responsible for the increase in mass-loss occurring about 1000 yr ago (Decin et al. 2006) or more recent ejections about 100 yr ago (Humphreys et al. 2024). Some outflows around VY CMa resemble the results of our simulations, however, the observed morphology is much more complex and requires an interplay of multiple effects. Our simulations, which were only meant as a proof of concept, were performed using simple treatments of radiative cooling and winds in the outflows, and therefore require more accurate prescriptions in follow-up studies. Improving the accuracy of our simulations will allow us to study the morphology of the outflows in greater detail, as well as produce synthetic observables that can be used for a better comparison with observations of VY CMa, providing a strong test for our hypothetical scenario.

## ACKNOWLEDGEMENTS

We thank the anonymous referee whose comments helped to improve this work. CL thanks Shazrene Mohamed for the fruitful discussions and suggestions and Mike Lau for the help in generating stellar profiles. This research has been supported by Horizon 2020 ERC Starting Grant ‘Cat-In-hAT’ (grant agreement no. 803158). The work of CL has been supported by the Charles University Grant Agency project no. 116324. The work of OP has been supported by the Charles University Research Program no. UNCE24/SCI/016. This work was supported by the Ministry of Education, Youth and Sports of the Czech Republic through the e-INFRA CZ (ID:90254). The simulations were performed using the Barbora cluster at IT4 Innovations and the allocations provided by the projects OPEN-27-60 and OPEN-30-50.

Software: NUMPY (Van Der Walt, Colbert & Varoquaux 2011); MATPLOTLIB (Hunter 2007); ASTROPY (Astropy Collaboration et al. 2013); MESA (Paxton et al. 2011); PHANTOM (Price et al. 2018); SPLASH (Price 2007).

## DATA AVAILABILITY

The output files from our simulations will be shared on reasonable request to the corresponding author. The video of the snapshots of the first interaction is available at <https://youtu.be/jcWOKyMayBE>.

## REFERENCES

- Astropy Collaboration, 2013, *A&A*, 558, A33  
 Aydi E., Mohamed S., 2022, *MNRAS*, 513, 4405  
 Beasor E. R., Davies B., Cabrera-Ziri I., Hurst G., 2018, *MNRAS*, 479, 3101  
 Bermúdez-Bustamante L. C. et al., 2024, preprint (arXiv:2401.03644)  
 Bermúdez-Bustamante L. C., García-Segura G., Steffen W., Sabin L., 2020, *MNRAS*, 493, 2606  
 Biehle G. T., 1994, *ApJ*, 420, 364  
 Bladh S., Höfner S., 2012, *A&A*, 546, A76  
 Blagorodnova N. et al., 2021, *A&A*, 653, A134  
 Bowen G. H., 1988, *ApJ*, 329, 299  
 Brandt N., Podsiadlowski P., 1995, *MNRAS*, 274, 461  
 Cannon R. C., 1993, *MNRAS*, 263, 817  
 Cannon R. C., Eggleton P. P., Zytzkow A. N., Podsiadlowski P., 1992, *ApJ*, 386, 206  
 Chen X., Han Z., Tout C. A., 2011, *ApJ*, 735, L31  
 Chen Z., Ivanova N., Carroll-Nellenback J., 2020, *ApJ*, 892, 110  
 Chevalier R. A., 2012, *ApJ*, 752, L2  
 Clayton M., Podsiadlowski P., Ivanova N., Justham S., 2017, *MNRAS*, 470, 1788  
 Darwin G. H., 1879, *Proc. R. Soc. London Ser. I*, 29, 168  
 Decin L., Hony S., de Koter A., Justtanont K., Tielens A. G. G. M., Waters L. B. F. M., 2006, *A&A*, 456, 549  
 Decin L. et al., 2016, *A&A*, 592, A76  
 Dinh-V-Trung, Bao N. T. T., Tien P. M., Hai B. V., Minh P. H., Khiem L. H., 2022, *AJ*, 164, 219  
 Dorda R., Patrick L. R., 2021, *MNRAS*, 502, 4890  
 Eggleton P. P., Kiseleva-Eggleton L., 2001, *ApJ*, 562, 1012  
 Ekström S. et al., 2012, *A&A*, 537, A146  
 Eldridge J. J., Stanway E. R., Xiao L., McClelland L. a. S., Taylor G., Ng M., Greis S. M. L., Bray J. C., 2017, *PASA*, 34, e058  
 Esseldeurs M. et al., 2023, *A&A*, 674, A122  
 Farmer R., Renzo M., Göteborg Y., Bellinger E., Justham S., de Mink S. E., 2023, *MNRAS*, 524, 1692  
 Ferland G. J. et al., 2017, *RMxAA*, 53, 385  
 Fragos T., Andrews J. J., Ramirez-Ruiz E., Meynet G., Kalogera V., Taam R. E., Zezas A., 2019, *ApJ*, 883, L45  
 Freytag B., Höfner S., 2023, *A&A*, 669, A155  
 Gagnier D., Pejcha O., 2023, *A&A*, 674, A121  
 Gagnier D., Pejcha O., 2024, *A&A*, 683, A4  
 Gail H. P., Sedlmayr E., 1988, *A&A*, 206, 153  
 Gail H.-P., Sedlmayr E., 2013, *Physics and Chemistry of Circumstellar Dust Shells*. Cambridge Univ. Press, Cambridge  
 Gail H. P., Keller R., Sedlmayr E., 1984, *A&A*, 133, 320  
 Gauger A., Gail H. P., Sedlmayr E., 1990, *A&A*, 235, 345  
 Gingold R. A., Monaghan J. J., 1977, *MNRAS*, 181, 375  
 Glanz H., Perets H. B., 2018, *MNRAS*, 478, L12  
 Glanz H., Perets H. B., 2021, *MNRAS*, 507, 2659  
 Goldberg J. A., Jiang Y.-F., Bildsten L., 2022, *ApJ*, 929, 156  
 González-Bolívar M., De Marco O., Lau M. Y. M., Hirai R., Price D. J., 2022, *MNRAS*, 517, 3181  
 Gordon M. S. et al., 2019, *AJ*, 157, 57  
 Gottlieb A. M., Eikenberry S. S., Ackley K., DeWitt C., Marco A., 2020, *ApJ*, 896, 32  
 Haubois X. et al., 2009, *A&A*, 508, 923  
 Hayashi C., Hoshi R., 1961, *PASJ*, 13, 442  
 Hinkle K. H., Lebzelter T., Fekel F. C., Straniero O., Joyce R. R., Prato L., Karnath N., Habel N., 2020, *ApJ*, 904, 143  
 Humphreys R. M., Helton L. A., Jones T. J., 2007, *AJ*, 133, 2716

- Humphreys R. M., Davidson K., Richards A. M. S., Ziurys L. M., Jones T. J., Ishibashi K., 2021, *AJ*, 161, 98
- Humphreys R. M., Richards A. M. S., Davidson K., Singh A. P., Decin L., Ziurys L. M., 2024, *AJ*, 167, 94
- Hunter J. D., 2007, *Comput. Sci. Eng.*, 9, 90
- Hut P., 1980, *A&A*, 92, 167
- Iaconi R., De Marco O., Passy J.-C., Staff J., 2018, *MNRAS*, 477, 2349
- Jacobson-Galán W. V. et al., 2022, *ApJ*, 924, 15
- Jermyn A. S. et al., 2023, *ApJS*, 265, 15
- Jones T. J., Humphreys R. M., Helton L. A., Gui C., Huang X., 2007, *AJ*, 133, 2730
- Kalogera V., 1996, *ApJ*, 471, 352
- Kaminski T., 2019, *A&A*, 627, A114
- Kamiński T., Gottlieb C. A., Young K. H., Menten K. M., Patel N. A., 2013, *ApJS*, 209, 38
- King A. R., 2009, *MNRAS*, 393, L41
- Klencki J., Nelemans G., Istrate A. G., Chruslinska M., 2021, *A&A*, 645, A54
- Kruckow M. U., Tauris T. M., Langer N., Szécsi D., Marchant P., Podsiadlowski P., 2016, *A&A*, 596, A58
- Kurfürst P., Pejcha O., Krtićka J., 2020, *A&A*, 642, A214
- Lada C. J., Reid M. J., 1978, *ApJ*, 219, 95
- Laibe G., 2014, *MNRAS*, 437, 3037
- Laibe G., Price D. J., 2012, *MNRAS*, 420, 2345
- Laibe G., Price D. J., 2014, *MNRAS*, 440, 2147
- Lamers H. J. G. L. M., Cassinelli J. P., 1999, *Introduction to Stellar Winds*. Cambridge Univ. Press, Cambridge
- Lau M. Y. M., Hirai R., González-Bolívar M., Price D. J., De Marco O., Mandel I., 2022, *MNRAS*, 512, 5462
- Levesque E. M., Massey P., Żytkow A. N., Morrell N., 2014, *MNRAS*, 443, L94
- van Loon J. T., Cioni M. R. L., Zijlstra A. A., Loup C., 2005, *A&A*, 438, 273
- Lucy L. B., 1971, *ApJ*, 163, 95
- Lucy L. B., 1976, *ApJ*, 205, 482
- Lucy L. B., 1977, *AJ*, 82, 1013
- Maccarone T. J., de Mink S. E., 2016, *MNRAS*, 458, L1
- Marchant P., Pappas K. M. W., Gallegos-Garcia M., Berry C. P. L., Taam R. E., Kalogera V., Podsiadlowski P., 2021, *A&A*, 650, A107
- Margutti R. et al., 2014, *ApJ*, 780, 21
- Mason B. D., Hartkopf W. I., Gies D. R., Henry T. J., Helsel J. W., 2009, *AJ*, 137, 3358
- Massey P., Neugent K. F., Ekström S., Georgy C., Meynet G., 2023, *ApJ*, 942, 69
- Mel'Nik A. M., Dambis A. K., 2009, *MNRAS*, 400, 518
- Metzger B. D., 2022, *ApJ*, 932, 84
- Moe M., Di Stefano R., 2017, *ApJS*, 230, 15
- Montez R. Jr, Kastner J. H., Humphreys R. M., Turok R. L., Davidson K., 2015, *ApJ*, 800, 4
- Neo S., Miyaji S., Nomoto K., Sugimoto D., 1977, *PASJ*, 29, 249
- Neugent K. F., 2021, *ApJ*, 908, 87
- Neugent K. F., Massey P., Morrell N. I., Skiff B., Georgy C., 2018, *AJ*, 155, 207
- Neugent K. F., Levesque E. M., Massey P., Morrell N. I., 2019, *ApJ*, 875, 124
- Neugent K. F., Levesque E. M., Massey P., Morrell N. I., Drout M. R., 2020, *ApJ*, 900, 118
- Nieuwenhuijzen H., de Jager C., 1990, *A&A*, 231, 134
- O'Gorman E. et al., 2015, *A&A*, 573, L1
- Ofek E. O. et al., 2014, *ApJ*, 789, 104
- Paczynski B., 1976, *Proc. IAU Symp. 73, Structure and Evolution of Close Binary Systems*, 73, 75
- Patrick L. R. et al., 2019, *A&A*, 624, A129
- Patrick L. R., Thilker D., Lennon D. J., Bianchi L., Schootemeijer A., Dorda R., Langer N., Negueruela I., 2022, *MNRAS*, 513, 5847
- Pavlovskii K., Ivanova N., 2015, *MNRAS*, 449, 4415
- Paxton B., Bildsten L., Dotter A., Herwig F., Lesaffre P., Timmes F., 2011, *ApJS*, 192, 3
- Paxton B. et al., 2013, *ApJS*, 208, 4
- Paxton B. et al., 2015, *ApJS*, 220, 15
- Paxton B. et al., 2018, *ApJS*, 234, 34
- Paxton B. et al., 2019, *ApJS*, 243, 10
- Pejcha O., Metzger B. D., Tomida K., 2016a, *MNRAS*, 455, 4351
- Pejcha O., Metzger B. D., Tomida K., 2016b, *MNRAS*, 461, 2527
- Pejcha O., Metzger B. D., Tyles J. G., Tomida K., 2017, *ApJ*, 850, 59
- Pejcha O., Calderón D., Kurfürst P., 2022, *MNRAS*, 510, 3276
- Pešta M., Pejcha O., 2023, *A&A*, 672, A176
- Podsiadlowski P., Cannon R. C., Rees M. J., 1995, *MNRAS*, 274, 485
- Price D. J., 2007, *PASA*, 24, 159
- Price D. J., 2012, *J. Comput. Phys.*, 231, 759
- Price D. J., Laibe G., 2015, *MNRAS*, 451, 813
- Price D. J. et al., 2018, *PASA*, 35, e031
- Quintana-Lacaci G., Vellilla-Prieto L., Agúndez M., Fonfría J. P., Cernicharo J., Decin L., Castro-Carrizo A., 2023, *A&A*, 669, A56
- Reichardt T. A., De Marco O., Iaconi R., Tout C. A., Price D. J., 2019, *MNRAS*, 484, 631
- Renzo M. et al., 2019, *A&A*, 624, A66
- Richards A. M. S. et al., 2014, *A&A*, 572, L9
- Ricker P. M., Timmes F. X., Taam R. E., Webbink R. F., 2018, *Proc. Int. Astron. Union*, 14, 449
- Röpke F. K., De Marco O., 2023, *Living Rev. Comput. Astrophys.*, 9, 2
- Sana H. et al., 2012, *Science*, 337, 444
- Schwarzschild M., 1975, *ApJ*, 195, 137
- Shenoy D. et al., 2016, *AJ*, 151, 51
- Shiber S., Soker N., 2018, *MNRAS*, 477, 2584
- Shiber S., Kashi A., Soker N., 2017, *MNRAS*, 465, L54
- Siess L., Homan W., Toupin S., Price D. J., 2022, *A&A*, 667, A75
- Smith N., 2011, *MNRAS*, 415, 2020
- Smith N., 2014, *ARA&A*, 52, 487
- Smith N., Humphreys R. M., Davidson K., Gehr R. D., Schuster M. T., Krautter J., 2001, *AJ*, 121, 1111
- Soker N., 2015, *ApJ*, 800, 114
- Suzuki A., Moriya T. J., Takiwaki T., 2019, *ApJ*, 887, 249
- Taberner H. M., Dorda R., Negueruela I., Marfil E., 2021, *A&A*, 646, A98
- Tauris T. M. et al., 2017, *ApJ*, 846, 170
- Telleschi A., Güdel M., Briggs K. R., Audard M., Palla F., 2007, *A&A*, 468, 425
- Theuns T., Jorissen A., 1993, *MNRAS*, 265, 946
- Thorne K. S., Zytow A. N., 1977, *ApJ*, 212, 832
- Tout C. A., Eggleton P. P., 1988, *MNRAS*, 231, 823
- Tout C. A., Zytow A. N., Church R. P., Lau H. H. B., Doherty C. L., Izzard R. G., 2014, *MNRAS*, 445, L36
- Tylenda R. et al., 2011, *A&A*, 528, A114
- Van Der Walt S., Colbert S. C., Varoquaux G., 2011, *Comput. Sci. Eng.*, 13, 22
- Vanture A. D., Zucker D., Wallerstein G., 1999, *ApJ*, 514, 932
- Verbunt F., Phinney E. S., 1995, *A&A*, 296, 709
- Vlasis A., Dessart L., Audit E., 2016, *MNRAS*, 458, 1253
- Vlemmings W. H. T. et al., 2017, *A&A*, 603, A92
- Wallerstein G., 1971, *ApJ*, 169, 195
- Webbink R. F., 1984, *ApJ*, 277, 355
- Wittkowski M., Hauschildt P. H., Arroyo-Torres B., Marcaide J. M., 2012, *A&A*, 540, L12
- Worley C. C., Irwin M. J., Tout C. A., Żytkow A. N., Fraser M., Izzard R. G., 2016, *MNRAS*, 459, L31
- Zahn J. P., 1977, *A&A*, 57, 383
- Zhang B., Reid M. J., Menten K. M., Zheng X. W., 2012, *ApJ*, 744, 23
- de Jager C., Nieuwenhuijzen H., van der Hucht K. A., 1988, *A&AS*, 72, 259
- Özel F., Freire P., 2016, *ARA&A*, 54, 401

## APPENDIX: RSG PROFILE

We need a realistic RSG profile to establish the boundary conditions (surface pressure and radius) and core size of our simple RSG interior. To obtain this stellar model, we use MESA v22.11.1 with the provided 20M\_PRE\_MS\_TO\_CORE\_COLLAPSE test case to evolve a 20  $M_{\odot}$  zero-

age main sequence star with metallicity  $Z = 0.02$  to the RSG phase without stellar winds. To produce a stellar model similar to VY CMa, we need to ensure that the stellar radius is large enough to reach very low densities in the outer envelope. As such, we looked for stellar evolution parameters for which the star expands as much as possible during the RSG phase. Similarly to Goldberg et al. (2022), we found that the largest envelopes result from a low mixing length coefficient in the H-rich envelope  $\alpha_H$ , i.e. less efficient convection. More specifically, we found that a model with  $\alpha_H = 1$  reaches about  $1150 R_\odot$  in the RSG phase while models with  $\alpha_H = 3$  only expand to  $1000 R_\odot$ .

We therefore choose to work with the model with the lowest mixing length and opt to analytically expand the stellar profile obtained to reach a radius of  $1500 R_\odot$ . This expansion is done following homology scaling relations, which are obtained by estimating the equations of stellar structure by including the conservation of mass distribution:

$$\frac{r_i(m)}{R_i} = \frac{r_f(m)}{R_f}. \quad (\text{A1})$$

The new surface pressure of the star  $P_f$  scales as follows:

$$P_f = P_i \left( \frac{M_f}{M_i} \right)^2 \left( \frac{R_i}{R_f} \right)^4. \quad (\text{A2})$$

We take the effective radius of the excised core to be half of the total radius of the star, which corresponds to a softening length of  $r_{\text{soft},i} = 287.5 R_\odot$  and a core mass of  $M_c = 13.75 M_\odot$  according to the MESA stellar profile. The radius of the core of the extended giant  $r_{c,f}$  is simply calculated using equation (A1).

Following this procedure, we expand a  $1150 R_\odot$  star with  $P_i = 212 \text{ dyn cm}^{-2}$  and  $r_{\text{soft},i} = 287.5 R_\odot$  to a  $1500 R_\odot$  star with  $P_f = 73 \text{ dyn cm}^{-2}$  and  $r_{c,f} = 375 R_\odot$ . These boundary conditions are then used to solve the equations of hydrostatic equilibrium to obtain a convectively stable stellar interior model as explained in appendix A of Lau et al. (2022). To construct this model, we use an ideal

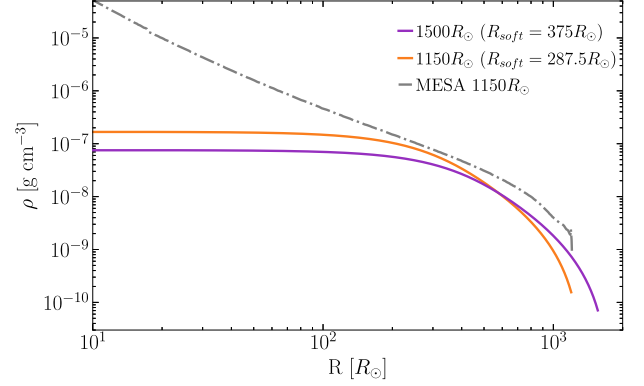


**Figure A1.** Comparison of the density profile of the RSG model obtained with MESA (grey line) with our simplified stellar profiles. The orange line shows the simplified profile calculated with the initial conditions from the MESA model, and the purple line shows the profile calculated with the expanded initial conditions.

gas equation of state with adiabatic index  $\gamma = 5/3$  and a uniform mean molecular weight  $\mu = 0.659$  (obtained from the average mean molecular weight in the envelope of the MESA model). In Fig. A1, we compare the detailed MESA model to the simple profiles obtained using initial conditions from MESA RSG and the extended initial conditions. Taken at face value, the density in the upper layers of the envelope is underestimated, and the density gradient is severely smoothed. This would lead to an underestimation of the outflow density and the impact of the grazing on the companion trajectory. However, the actual density profile near and above the photosphere is affected by pulsations and wind launching and likely significantly differs from a simple 1D stellar model.

This paper has been typeset from a  $\text{\TeX}/\text{\LaTeX}$  file prepared by the author.